Materials and Design 163 (2019) 107539

Contents lists available at ScienceDirect

Materials and Design

journal homepage: www.elsevier.com/locate/matdes

Thermal design, optimization and additive manufacturing of ceramic regular structures to maximize the radiative heat transfer

M. Pelanconi [a], M. Barbato [a], S. Zavattoni [a], G.L. Vignoles [b], A. Ortona [a,*]

[a] University of Applied Sciences of Southern Switzerland, DTI – Department of Innovative Technologies via Cantonale 2C, 6928 Manno, Switzerland
[b] University of Bordeaux-CNRS-Safran-CEA Laboratory for ThermoStructural Composites (LCTS) Allée de La Boétie 3, 33600 Pessac, France

HIGHLIGHTS

- An alumina tubular heat exchanger (dia. 20 mm, length 500 mm) with cellular architectures was realized and tested in flowing air at 773, 873 and 973 K
- Periodic ceramic architectures with varying cell size distribution (2–4 mm) were designed and produced by Additive Manufacturing.
- The lattice improves the heat transfer of 160÷280% in respect of the empty tube
- The RDCS lattice yields the highest air outlet temperature (957 K) in respect of the empty tube (466 K)
- The RICS lattice shows the worst performance (841 K), the S geometry shows an intermediate behavior (925 K)

GRAPHICAL ABSTRACT

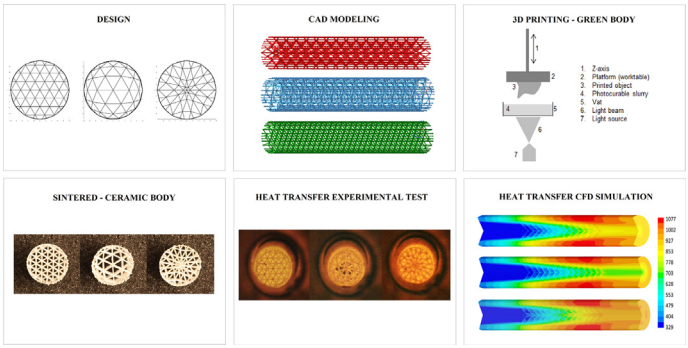

ARTICLE INFO

Article history:
Received 2 July 2018
Received in revised form 3 December 2018
Accepted 4 December 2018
Available online 6 December 2018

Keywords:
Porous ceramic
Alumina
Heat exchange
Additive manufacturing

ABSTRACT

The present study is focused on the application of a ceramic tubular high temperature heat exchanger with engineered cellular architectures. Thermal design and optimization to maximise the radiative heat transfer has been investigated both experimentally and computationally. Numerical models were designed involving various arrangements of cells and their different sizes (while the total heat transfer area remains constant). They were 3D-printed by Stereolithography (SLA) and subsequently sintered. Heat transfer tests were performed both with a high temperature pressure drop test and by CFD simulations on 2D and 3D models. The computational results agree with the experimental data. We found that radial heat transfer in a tube increases by 160% to 280%, if a ceramic lattice is inserted, in respect of an empty tube. Moreover, the arrangement of cells and their size significantly influences the radiative heat transfer showing (for a given array) its top performances above 773 K. Geometries with large cells outside and small cells inside in the radial direction allow radiation to penetrate better through the core of the porous body. With this engineered ceramic lattices it is possible to reduce the tube length by one third to obtain more compact heat exchangers than an empty tubular solution.

1. Introduction

Heat exchangers made of ceramic materials [1] are used in several high-temperature new applications such as: concentrated solar energy plants, industrial burners and high temperature heat storage [2]. They

* Corresponding author.
E-mail address: alberto.ortona@supsi.ch (A. Ortona).

https://doi.org/10.1016/j.matdes.2018.107539

Nomenclature

P_{abs}, [Pa] inlet air pressure
ΔP, [Pa] pressure drop
ΔP_{3D}, [Pa] pressure drop in 3D domain
ΔP_L, [Pa] pressure drop with a lattice
ΔP_{ET}, [Pa] pressure drop with ET
T, [K] temperature
ΔT, [K] difference of temperature
T_{inlet}, [K] inlet air temperature
$T_{inlet\text{-}3D}$, [K]
inlet air temperature in 3D domain
$T_{ext\text{-}c}$, [K] central outer tube temperature
$T_{out\text{-}ext}$, [K]
outlet wall temperature of the tube
T_{outlet}, [K] outlet air temperature
$T_{outlet\text{-}mwa}$, [K]
outlet air temperature (mwa)
$T_{outlet\text{-}mwa\text{-}3D}$, [K]
outlet air temperature of 3D model (mwa)
Q, [W] heat flux transfer to air
Q_L, [W] heat flux transfer to air with a lattice
Q_{ET}, [W] heat flux transfer to air with ET
G_Q, [%] gain of the heat transfer over ET
$I_{\Delta P}$, [%] increase in pressure drop over ET
Re, [−] Reynolds number
Re_p, [−] pore Reynolds number
W, [m/s] air velocity in the tube
w_p, [m/s] air velocity in the pore
V_s, [m^3] solid volume
V_t, [m^3] total volume
A_s, [m^2] surface area
k, [1/m] absorption coefficient

Acronyms
S Standard lattice
RICS Radially Increasing Cell Size
RDCS Radially Decreasing Cell Size
ET empty tube
HTPD High Temperature Pressure Drop machine
mwa mass-weighted average

Greek letters
σ, [1/m] Scattering coefficient
μ, [Pa s] Dynamic viscosity
ρ, [kg/m^3] Mass Density
φ, [−] Porosity
ε, [−] Emissivity

Subscripts
C, [m] cell diameter
p, [m] pore diameter
s, [m] strut diameter
D, [m] lattice diameter
L, [m] lattice length along Z axis
Nz, [−] number of cells along Z axis

outperform their metallic competitors at high temperatures and in corrosive environments [3].

Ceramic heat exchangers with different geometrical features have been successfully produced and tested, namely: tubes, plates, finned and channelled [4]. Tubular heat exchangers [5] are characterized by a low thermal efficiency, but their heat exchange performance [6] can be enhanced with turbulators such as: spiral tapes, fins and solid foams. The drawback of this technique is that pressure drop increases, but the overall efficiency of the system remains profitable.

Ceramic periodic architectures belong to the family of cellular ceramics, which gathers reticulated porous structures (foams), honeycombs and lattices. Unlike foams, lattices have an ordered 3D structure consisting of an interconnected network of repeatable dimensional arrangements [7] called "unit cells". Several types of unit cell can be designed and manufactured [8], among them: octet, cube, hexagon, tetrakaidekahedron. As an example, active and passive thermal protections for re-entry vehicles were optimised thanks to a combined study on the thermal and thermo-mechanical behaviour under real re-entry conditions [9].

In the last years, reticulated porous materials have been employed in tubular components [10] with the aim of enhancing the overall heat transfer by exploiting suitable cells morphology [11].

The arrangement of the cells can be controlled through several parameters, such as: size, cell type and orientation. Numerous studies have been carried out to evaluate their effects when varying one parameter at a time both experimentally and numerically [12]. The common goal of these research efforts was to obtain a trade-off between heat transfer and pressure drop [13]. Furthermore, macro porous lattices are characterized by a high porosity (>90%) that favours heat transfer, radiation propagation, pressure drop and fluid dispersion [14].

For heat conduction, in a previous paper [15], the effect of tetrakaidekahedra morphological features, such as cell inclination, ligament radius and tapering, was analysed. Wu et al. [16] investigated convective heat transfer by varying average cell size and cells number and Ferrari et al. [17] have demonstrated that the increase of volume fraction of cells generates an increase in the heat transfer, because of the larger heat transfer area.

In this kind of high temperature applications, the dominant heat transfer mechanism is thermal radiation and studies have been performed on radiative properties of different foams using tomographic images and stereoscopic micrographs [18]. Thermal radiative behaviour has also been studied in respect of foams porosity [19,20] and trying to couple conduction and radiation in cellular ceramics of different architectures [21]. Wu et al. [22] investigated the radiative heat transfer between air flow and ceramic foams to optimise volumetric solar air receiver performances, both experimentally and numerically, showing that the mean cell size has a dominant effect on the temperature field. Additionally, Haussener et al. [23] proposed a foam design for enhancing the effective of heat and mass transport properties of porous ceria samples for solar thermochemical fuel generation.

In this paper, ceramic lattice thermal design and optimization to maximise the radiative high-temperature heat transfer has been investigated both experimentally and computationally (CFD). The study dealt with three types of ceramic lattices with rotated cubic cells. The lattices have the same surface area: S lattice with uniform cell size, RICS lattice with a "Radially Increasing Cell Size" and RDCS lattice with a "Radially Decreasing Cell Size".

Heat transfer tests were performed with a heated ceramic tube through which ambient temperature was forced to pass, in parallel CFD simulations of the experiments were carried out in 2 and 3 dimensions. Three different outer temperatures and three air-flow rates were considered and benchmarked with the heat transfer of an empty tube. This investigation shows the best performance of the RDCS design above 773 K.

2. Lattices generation

2.1. Lattices generation algorithm

Lattice geometries were generated through a parametric algorithm coded using MATLAB R2017 (MathWorks. Natick, Massachusetts, USA). The output of the program is an array of spheres and cylinders. This routine allows generating user-defined lattice topology acting on control parameters such as: outer dimensions, number of cells in the

volume, cell type and size, struts diameter and distortion coefficient (used to vary the cells size within the lattice).

Fig. 1 shows the three lattices designed and produced in this work:

- Standard (S) lattice with a constant unit cell size of 4 mm.
- Radially Increasing Cell Size (RICS): lattices having an external 4 mm cell size increasing inward to 8 mm in the centre.
- Radially Decreasing Cell Size (RDCS) lattices having an external 4 mm cell size decreasing inward to 2 mm in the centre.

The lattices denomination was given according to the heat flux direction, i.e. radially from the outside to the inside of the geometry. The lattices were generated from the S lattice by inserting a distortion coefficient that creates a radial coordinate stretch: +0.8 for RICS and −0.8 for RDCS (positive: inward growth rate; negative: inward decreasing rate).

Cylindrical samples with 20 mm external diameter and 0.5 mm struts diameter were generated. Lattices length was kept at 100 mm (corresponding to 15 cells along the Z axis); to compare results, the surface area and porosity were kept similar in all cases.

The commercial software program NX 10.0 (Siemens. Munich, Germany) was then used to scale the structure of the lattices according to the 3D printer resolution and the sintering shrinkage. The structures sizes have been scaled up by 10% in order to obtain cylindrical samples with 22 mm external diameter, 110 mm height and 0.55 mm struts diameter. The lattices were comprised with cubic unitary cells, rotated 45° on each axis (called "C111"), with the main diagonal of the cube parallel to the cylinder axis (Z axis). The geometry of the unit cell is shown in Fig. 2.

Table 1 shows the geometrical characteristics of the reference lattice structures under investigation.

Table 1
Lattice characteristics both of the CAD models without scaling up and final sintered part.

		S	RICS	RDCS
V_s	[mm^3]	1474	1351	1499
V_t	[mm^3]	31,416	31,416	31,416
Φ	[−]	0.953	0.957	0.952
A_s	[mm^2]	11,807	10,677	11,996
L	[mm]	103.9	103.9	103.9
D	[mm]	4	From 2 to 8	From 4 to 2
N_z	[−]	15	15	15

2.2. Lattices manufacturing

The lattices were manufactured through the Stereolithography (SLA) technique, which is an additive manufacturing (AM) process that allows the fabrication of three-dimensional polymeric parts with UV radiation. SLA can be used for processing ceramic powders providing a suitable suspension into a liquid resin and an appropriate printing setup [8–25]. The process exploits the photopolymerization of a slurry consisting of acrylic resin TPGDA 56.8 vol% (Allnex, Luxenburg, Luxenburg) mixed with alumina powders (D90: 2 μm) 42 vol% (Nabaltec, Schwandorf, Germany) and UV photo initiator, Irgacure 819 1.2 wt% (BASF, Ludwigshafen, Germany). The slurry was thoroughly mixed by ball mixing for 24 h with zirconia balls D = 8.5 mm, 30 vol% [26]. The object was then built layer by layer projecting with UV light a sequence of images obtained by slicing the 3D-CAD file (.STL file). Printing was performed with a stereo lithographic 3D printer (RobotFactory 3DL Printer HD2.0. Robot Factory SRL, Mirano, Italy). The main printing parameters adopted in this study are reported in Table 2. Each lattice underwent a 15-min post-curing treatment in an

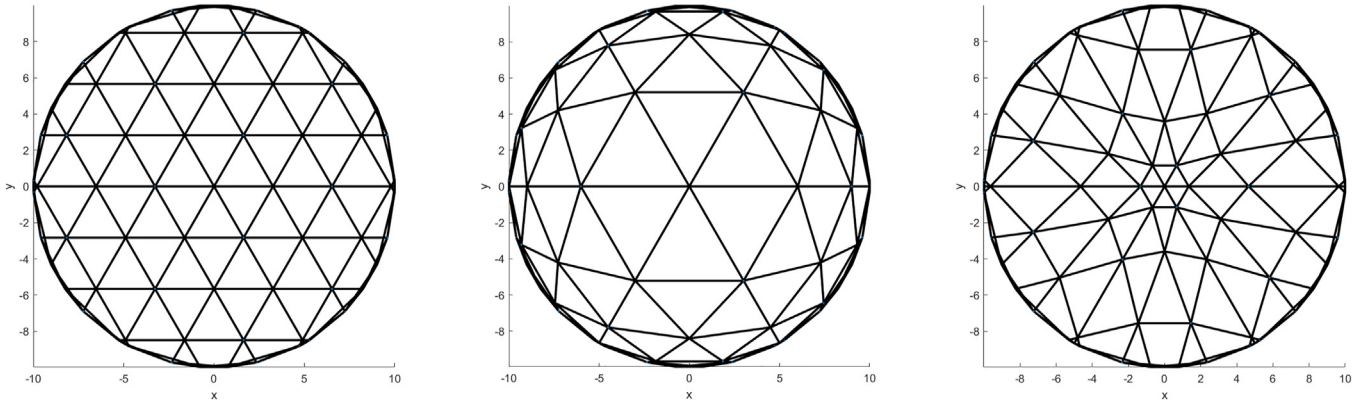

Fig. 1. From left to right: S, RICS and RDCS lattices (XY view).

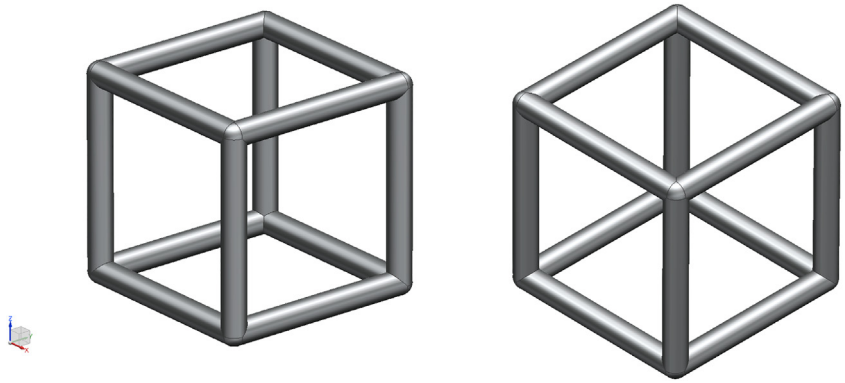

Fig. 2. Unitary cell of the rotated cube C111. On the left (in isometric) view and on the right (in frontal view).

Table 2
Main printing parameters exploited to realize the lattice samples.

Shrinking	≅10%
Print time	≅60 min per lattice
Number of layers	≅500 per lattice
Inter-layer distance	0.05 mm
UV projection time	5 s. for the base, 1 s. for the struts

UV oven, to increase their mechanical resistance. The polymerized resin in the 3D printed body was subsequently removed through a thermal treatment in air consisting of thermal de-binding at 673 K and sintering at 1873 K for 2 h [27]. The final ceramic product has a bulk density of 3720 kg/m^3 and then, according to [28], a thermal conductivity of 29 W/mK at room temperature. Due to printing volume limitations, S, RDCS and RICS lattices were made in three pieces of about 33 mm length each, to obtain upon stacking, a total length of 100 mm. Fig. 3 shows flowchart of the manufacturing process developed and Fig. 4 shows the Al_2O_3 lattices produced.

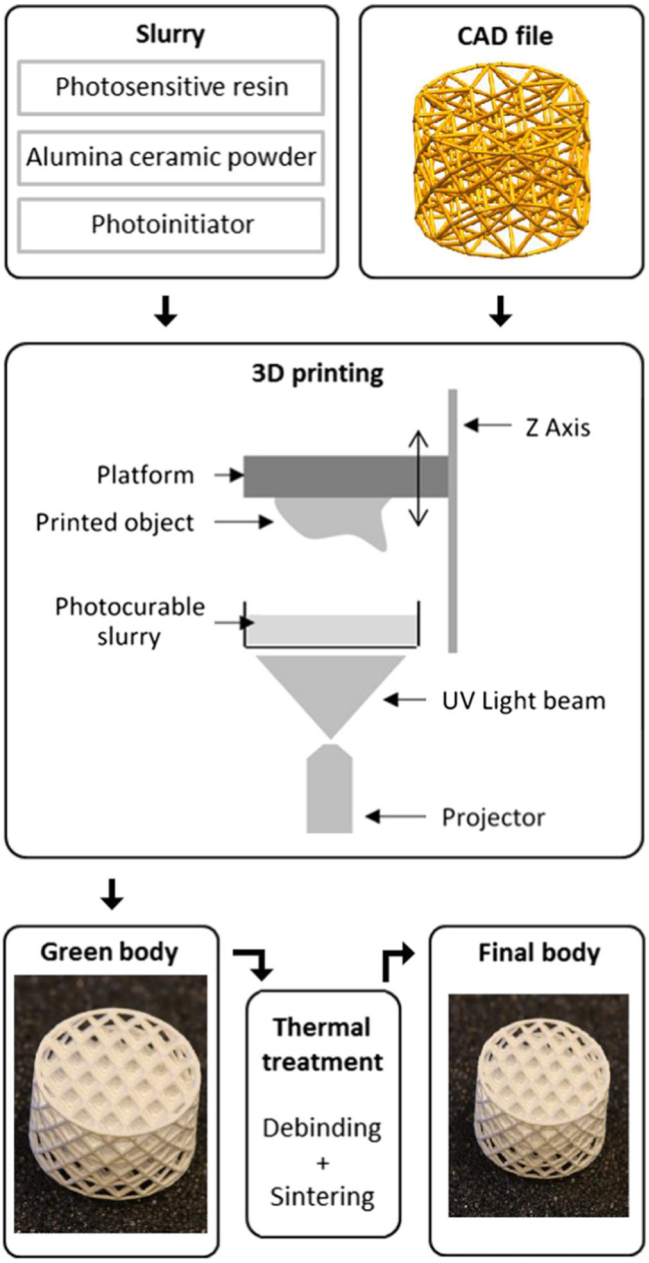

Fig. 3. Flowchart of the manufacturing process.

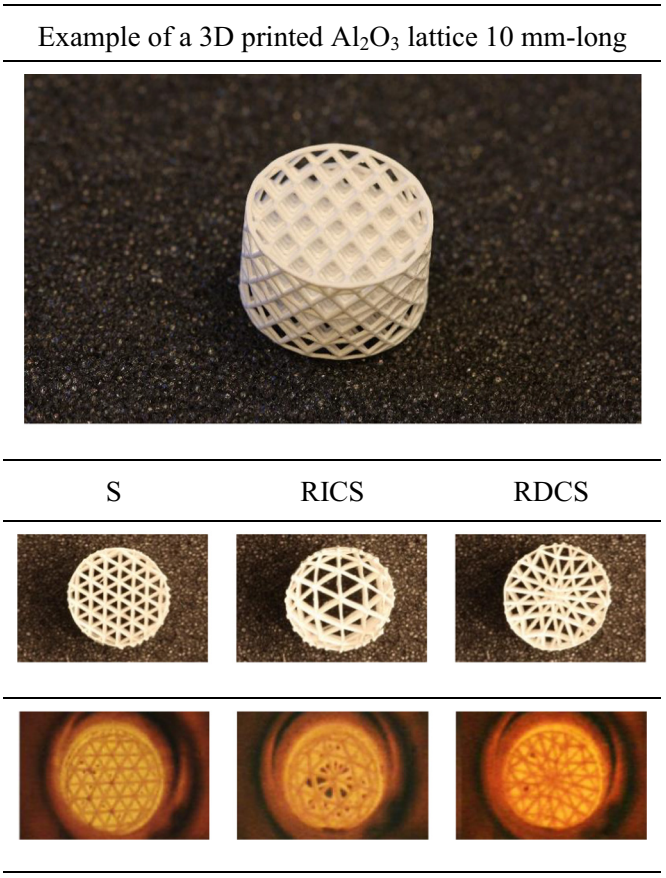

Fig. 4. 3D printed Al_2O_3 lattices after sintering and during high temperature tests at 973 K.

3. Experimental method

Tests were performed using the High Temperature Pressure Drop (HTPD) apparatus developed at SUPSI.

This apparatus, schematically represented in Fig. 5, calculates the heat transfer between the hot walls and cold air passing through a ceramic tube (with or without porous inserts) along with the pressure drop at the inlet and the outlet of the tube. The tube passes through a furnace (Type XTube, XERION Advanced Heating Ofentechnik GmbH, Freiberg, Germany) preset at constant temperature. When inserted, the lattices were in contact with the inner tube wall. The ceramic tube (Alumina C799, SCERAM Ceramics, Champagne au Mont d'Or, France) has a length of 500 mm, an internal diameter of 20 mm and an external diameter of 27 mm. The insulation around the tube is made of Alumina (Duoflet 1700/130, Duotherm Stark Isoliersysteme GmbH & Co KG, Mechernich, Germany).

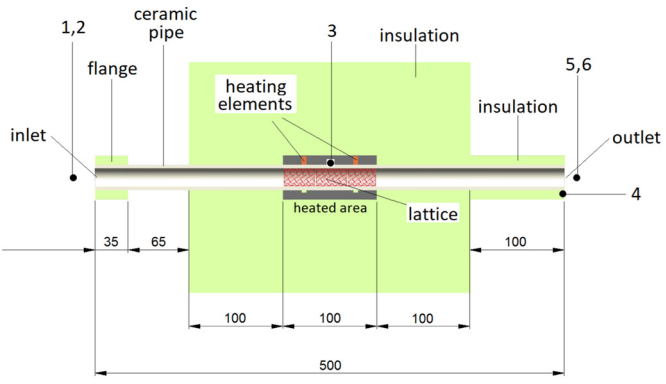

Fig. 5. Schematic of the HTPD machine (units: mm). The numbers refer to the sensors installation (Table 3).

Table 3
Measured quantities on HTPD machine.

1	Inlet air pressure	P_{abs}
2	Inlet air temperature	T_{inlet}
3	Central outer tube temperature	T_{ext-c}
4	Outlet wall temperature of the tube	$T_{outlet-ext}$
5	Outlet air temperature	T_{outlet}
6	Pressure drop	ΔP

Table 3 reports the quantities measured with the HTPD apparatus. The measurement equipment is composed by the following sensors:

- Self-assembled Type K Thermocouples (calibration: 0–100 °C; accuracy: ±0.5 °C). In order to avoid irradiation, the sensors were shielded with a protective felt.
- Digital pressure gauges: DPGM409-025HG, OMEGA Engineering INC, Norwalk, USA (5-point NIST Traceable Calibration; accuracy: ±0.08% of full scale).
- Digital differential pressure gauges: DPGM409-025HDWU, OMEGA Engineering INC, Norwalk, USA (5-point NIST Traceable Calibration; accuracy: ±0.08% of full scale).
- Mass flow controller: SMART6 GSC-C5, Vögtlin Instruments GmbH, Aesch, Switzerland (real gas calibration: METAS standard, Federal Office of Metrology, Switzerland; accuracy: ±0.3% of full scale).

The experimental conditions were: ambient temperature of 298 K and, air temperature at the inlet of the tube of 293–298 K and atmospheric pressure of 98 kPa. The experiments were performed setting three furnace temperatures: 773 K, 873 K, 973 K and three air flow velocities corresponding to the following Reynolds numbers: 745 (0.6 m/s), 1′490 (1.2 m/s) and 2′235 (1.8 m/s). Fig. 4 shows the three ceramic architectures under investigation during high temperature tests at 973 K.

4. Numerical simulation

Due to the extreme complication in modelling the behaviour of the full experimental system we decided to split simulations in two. We first performed 2D CFD simulations fixing the airflow rates and temperatures (the same of the experimental tests). This task was performed to evaluate the heat transfer and the pressure drop of two configurations: the empty tube and the tube with the S lattice. This work was necessary to calculate the temperature field of the tube (inside and outside) before the hot zone of the furnace.

3D CFD simulations were then performed to detail the thermo fluid dynamic behaviour of the air inside S, RICS and RDCS lattices. Due the huge computational effort, these local simulations were performed only for one Reynolds number.

4.1. Computational domain

A 2D and 3D CFD-based approach was followed to replicate the experimental tests performed on all the reference lattice structures under investigation. For the 2D axisymmetric CFD analysis, the computational domain (see Fig. 6) was constituted by the heated ceramic tube and by the lattice structure, the latter being represented as an equivalent homogeneous porous medium.

Conversely, in the case of the 3D CFD analysis, the computational domain was limited to the central region of the heated pipe containing the lattice structure accurately modelled. Based upon the symmetric characteristics of both the lattice topology (diagonal of the unit cell oriented along the airflow direction) and the fluid flow, the extension of the computational domain was limited to 60°, assuming therefore a symmetric boundary condition to replicate the whole geometry. The overall length of the computational domain was 200 mm. The lattice structure was always located in the middle of the computational domain, the latter also including the ceramic tube.

Due to meshing issues, the contact regions between the lattice and the inner surface of the tube were removed. According to this geometric simplification, the heat transfer mechanisms available between the lattice structures and the ceramic pipe were thermal radiation and convection.

4.2. Computational grid generation

As far as the 2D axisymmetric computational domain is concerned, a grid (mesh) sensitivity analysis was performed to determine the minimum number of elements that ensures grid-independent results. Three different computational grids were prepared: coarse (47′000 quad. elements), normal (190′000 quad. elements) and refined (750′000 quad. elements). According to the mesh sensitivity analysis results for the heat flux and the pressure drop, the normal computational grid was assumed as reference for all the 2D CFD simulations.

The reference lattice structures were also analysed by means of 3D CFD simulations. In order to obtain a good quality mesh, major simplifications to the original lattices have been applied (such as: eliminating the external linking struts and introducing additional chamfers). However, the intrinsic geometrical complexity of these structures required computational grids of several millions tetra/prism elements. Since heat transfer and fluid flow have to be accurately modelled, an inflation layer (4 layers of 0.1 mm total thickness and growth rate of 1.2) was imposed from all the solid surfaces of the lattice structures towards the fluid domain. Table 4 summarizes the main characteristics of all the computational grids generated.

4.3. Numerical modelling

The developed numerical steady state model solves mass, momentum and energy conservation equations exploiting the finite-volume

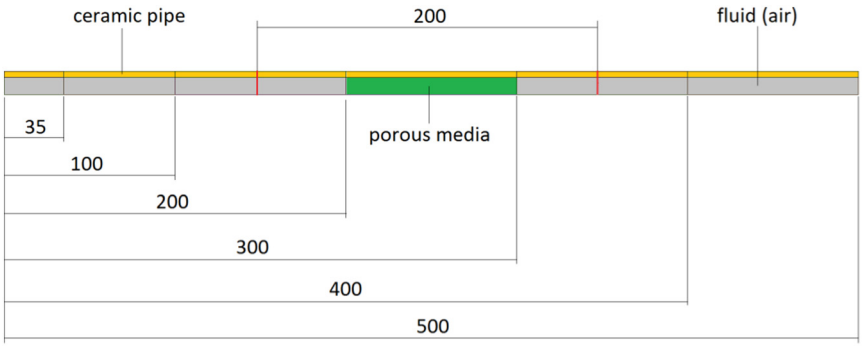

Fig. 6. 2D numerical domain (units: mm).

Table 4
Characteristics of the generated computational grids.

Reference geometry	Elements type	Number of elements	Maximal skewness
2D	Quadrilateral	0.19e06	1.34 e-10
S, RICS, RDCS (3D)	Tetra/Prism	50e06	0.95

Table 5
Porous media modelling: cell diameter, porosity, absorption and scattering factors for the S lattice.

D_c [mm]	φ [−]	k [1/m]	σ [1/m]
4	0.9531	14.07	21.11

Table 6
Experimental measurements for pressure drop and airflow velocity correlation for S lattice.

w [m/s]	ΔP [Pa]
0.85	5.48
1.67	14.41
2.50	27.40

method [29] through ANSYS Fluent v17.1 (ANSYS, Pittsburgh, PA, USA). Radiative heat transfer is also accounted for through the grey discrete ordinates (DO) radiation model that solves the radiative transfer equation for a finite number of discrete solid angles [30]. The mentioned balance equations are well known; therefore they will not be recalled hereafter for the sake of brevity.

The so-called "pore Reynolds number approach", suggested by Ashby et al. [31], was applied to evaluate the flow regime through the lattice structures:

$$Re_p = \frac{\rho D}{\mu} w_p = \frac{\rho D}{\mu} \frac{W}{\varphi} \tag{1}$$

With this formulation, the threshold of the laminar-turbulent transition is $Re_p = 150$[20]. In low velocity cases, the Re_p was about 100, indicating that the flow through the lattice structures can be assumed laminar. In other cases, the Re_p was about 350, indicating a turbulent flow. The latter simulations were then carried out both with a laminar model and with a turbulent model (the *k-ω* Shear Stress Transport model), and no practical differences were appreciated.

4.4. 2D CFD simulations – lattice structures modelling

For all the 2D CFD simulations performed, the lattice structures were modelled exploiting the equivalent porous media approach (under the assumption of local thermal equilibrium [29]) and therefore, they were considered as continuous media [30].

Concerning heat transfer by thermal radiation, the optical properties of the lattice structures, i.e. absorption coefficient (k) and scattering coefficient (σ), were also implemented in the model. These two coefficients, considered homogeneous and independent from the radiation wavelength, were computed according to Vafai's model [22–32] summarized by Eqs. 2 and 3. The alumina emissivity (ε) was set to 0.8, by averaging the spectral normal emittance in the infrared wavelength spectrum, according to reference [33].

The resulting values are reported in Table 5.

$$k = \frac{3}{2D} \varepsilon (1-\varphi) \tag{2}$$

$$\sigma = \frac{3}{2D} (2-\varepsilon)(1-\varphi) \tag{3}$$

To account for the pressure drop given by the real lattice structures, in the porous media approach, a source term is added to the momentum equation, which generates a pressure gradient proportional to the fluid velocity. The source term is composed of two parts: a viscous loss term and an inertial loss term proportional to the fluid velocity and the square of the fluid velocity respectively. To quantify these two coefficients for each lattice structure, an additional experimental campaign was conducted with the aim of correlating air-flow velocity and pressure drop. Table 6 summarizes the experimental data obtained. The

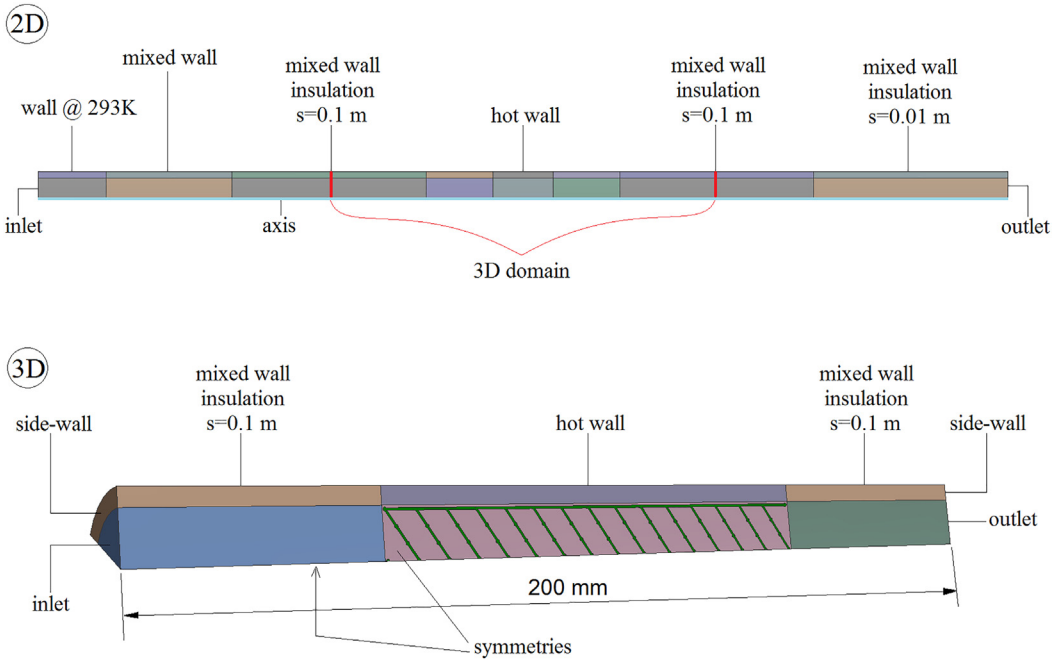

Fig. 7. Boundary conditions applied for the 2D and the 3D numerical analysis.

data points were very well fitted ($R^2 = 0.99998$) by the Darcy-Forchheimer equation:

$$\frac{\Delta P}{L} = \frac{w\,\mu}{\alpha} + \frac{w^2 \rho}{\beta} \tag{4}$$

where α is the permeability (m^2) and β is the passability (m). We found $\alpha = 6 \cdot E\text{-}7\ m^2$, which is consistent with a pore diameter size of ~0.004 m. The passability coefficient was found to be 0.0145 m.

4.5. Boundary conditions

The boundary conditions applied to the model are closely related to the experimental set up and test conditions described in Section 3.

A constant heat flux boundary condition was applied on the outer surface of the tube and the resulting temperature, at the centre of the heated zone, was compared with that of the experimental tests.

The lattice structures were tested at three different temperatures, 773 K, 873 K, 973 K, in order to better observe the influence of thermal radiation on the heat transfer. Three air flow velocities corresponding to the following Reynolds numbers were defined for each lattice temperature: 745 (0.6 m/s), 1′490 (1.2 m/s) and 2′235 (1.8 m/s). At the outlet section, a constant relative pressure boundary condition was imposed. In the vicinity of the heated zone, the ceramic pipe was isolated, while in the inlet there was a free wall and a wall with a cold flange, as shown in Fig. 7.

Heat losses were also accounted for by means of a mixed boundary condition of convection and thermal radiation. The heat losses by natural convection were characterized by a heat transfer coefficient of 6 W/m^2K, whereas those given by thermal radiation were characterized by a superficial emissivity of the pipe of 0.9. The external temperature was taken as 298 K.

Concerning the 3D domain, the inlet conditions of the airflow were taken from the 2D model.

For both the 2D and the 3D simulations, a fully developed inlet airflow was assumed.

4.6. Numerical details

Since the Mach number was well below 0.3 for all the experimental tests performed, the air was assumed as an incompressible ideal gas. This means that its density variation with temperature is treated with a segregated model, while the mass density was calculated with the ideal gas equation. Temperature-dependent thermophysical properties of air were considered with values gathered from reference [34]. Concerning the solid materials, i.e. lattice, ceramic pipe and insulation, their thermophysical properties (summarized in Table 7) were measured by ourselves or obtained from the suppliers datasheets and taken as constant values, i.e. independent of temperature.

The solution method was set according to the SIMPLE scheme [29], which is a pressure-based approach. A second order upwind scheme was used for the spatial discretization of the transport equations, with the gradients computed exploiting a Green-Gauss node-based method.

Besides monitoring the evolution of representative properties such as air outlet temperature, airflow velocity, lattice temperature, convergence of the iterative process was considered achieved when residuals were below 10^{-5} for momentum and continuity equations, 10^{-8} for energy and 10^{-6} for radiative specific intensity.

Table 7
Material properties.

Material	Density [kg/m³]	Thermal conductivity [W/(m K)]	Specific heat [J/(kg K)]
Lattice	3′850	29 (@293 K)	880
Ceramic pipe	3′850	29 (@293 K)	880
Insulation	130	0.24 (@1′273 K)	880

5. Results & discussions

The experimental results report the heat transfer and pressure drop behaviour of the lattice structures compared to the empty tube. The assessment between experimental tests and CFD simulations was performed to verify the validity and the accuracy of the numerical approach. According to Eq. 4 the experimental data points were used to obtain a quadratic fit of the pressure drop and the air outlet temperature in respect of the gas velocity. Table 10 summarize the experimental, 2D and 3D results.

5.1. Behaviour of S in comparison with ET

Fig. 8 shows the comparison between CFD simulations and experiments on the empty tube and the tube with the S lattice, in terms of air outlet temperature and pressure drop. The experimental outlet

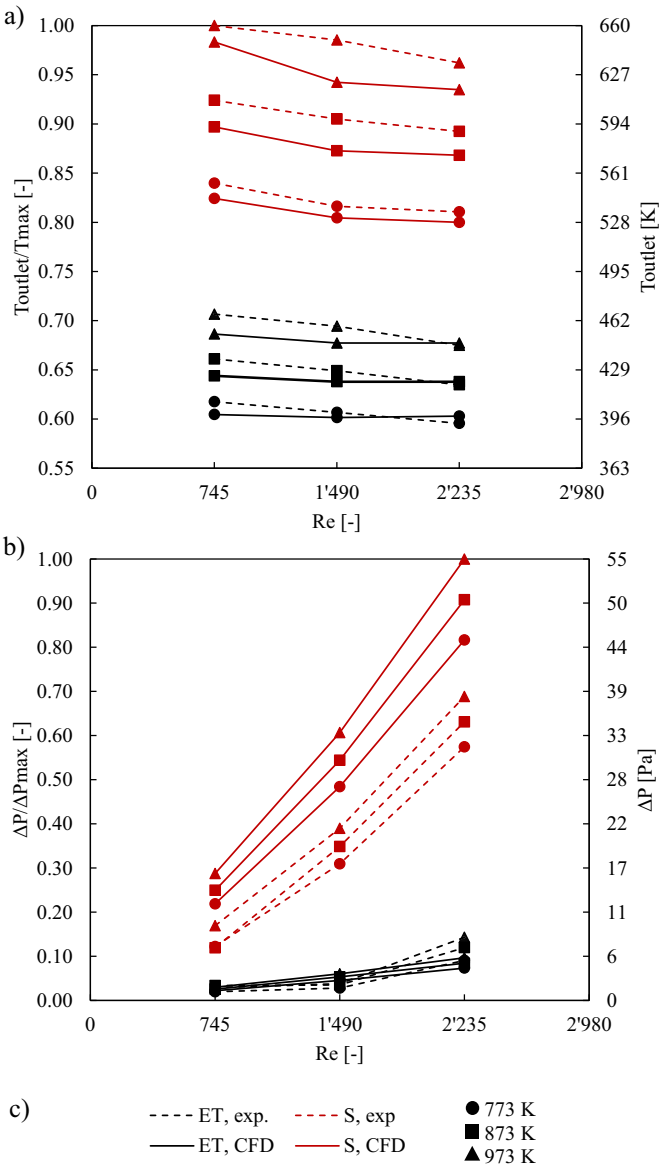

Fig. 8. Tube with Standard lattice (S) vs empty tube (ET): experimental tests and 2D simulations results. a) Outlet air temperature vs. Reynolds number ($T_{max} = 660$ K); b) Pressure drop vs. Reynolds number ($P_{max} = 55$ Pa); c) Legend.

Table 8
Gain on heat transfer and increase of pressure drop for Standard lattice compared to ET.

Re	T_{ext-c}	G_Q	$I_{\Delta P}$
[−]	[K]	[%]	[%]
745	773	192%	897%
745	873	173%	874%
745	973	161%	864%
1′490	773	253%	963%
1′490	873	232%	922%
1′490	973	218%	902%
2′235	773	279%	1′016%
2′235	873	262%	976%
2′235	973	243%	935%

temperature (Fig. 8a) is slightly higher than the one given by the numerical model, because the thermocouple located at the outlet section of the pipe was not shielded and therefore, it captured radiation from the centre of the tube. This behaviour also explains why, when the lattice was inserted, the difference was larger. The sensor receives more radiation due to the high surface area of the lattice reflecting the radiation towards the outlet of the tube. According to the results, the ratio between the power removed by the airflow and the input power from the furnace increased upon increasing the mass flow rate, indicating therefore a further improvement on the heat transfer between pipe and airflow.

As expected Fig. 8b, shows that the pressure drop in the tube with the lattices is 6–10 times larger than the one measured for the empty tube. Its gradient (in respect of *Re*) is even higher: this is due to the presence of the solid material that obstructs the passage of the fluid (despite the very high porosity of the lattice). Furthermore, the pressure drop increases when increasing the temperature of the wall at a given flow rate: this is due to both the increase of (i) air viscosity with temperature and (ii) airflow velocity caused by decreased density.

In terms of pressure drop, a good agreement can be observed between experimental data and simulation results in the case of empty tube. In the case of the lattices, a difference between experiments and simulation is evident. This is due to the not accurate inputs fed into Eqs. (2)–(4) which were calculated with a limited number of experiments. We did not perform further tests since we judged the accuracy of their absolute values sufficient to perform (by 3D CFD) a relative comparison between the different lattices.

For the performance comparison between ET and S lattices, two factors have been calculated: the relative gain on heat transfer of a tube with a lattice compared to an ET and the relative increase of pressure drop of a tube with a lattice compared to an ET, with eq. 5 and Eq. 6 respectively. Table 8 summarizes the results obtained in the two factor calculations for the S lattice.

$$G_Q = \left(\frac{Q_L - Q_{ET}}{Q_{ET}}\right) \tag{5}$$

$$I_{\Delta P} = \left(\frac{\Delta P_L - \Delta P_{ET}}{\Delta P_{ET}}\right) \tag{6}$$

The aerothermal efficiency equation [35] can be used to estimate the heat exchanger behaviour, however it cannot be rigorously applied as the lattice in this paper are very intricate structures. The information that emerges from Eqs. 5 and 6 are of the same meaning.

The lattice integrated in the tube greatly improves the heat transfer. The highest gain of heat transfer is produced at 773 K and with the Reynolds number of 2′235. It decreases according to the air mass flow rate, which is directly proportional to the heat flux. Concerning the pressure drop, the drawback of having the lattice structures into the pipe translates into a relevant increase with respect to the empty tube.

5.2. S, RICS and RDCS lattices behaviour

The study of the S, RICS and RDCS lattices was performed both through CFD simulations and experimental tests. The experiments were executed on the full pipe (500 mm), while the 3D-CFD simulations apply only to its hot zone (200 mm). In Figs. 9 and 10, we show that the relative behaviour is similar. The lattices were studied at one Reynolds number.

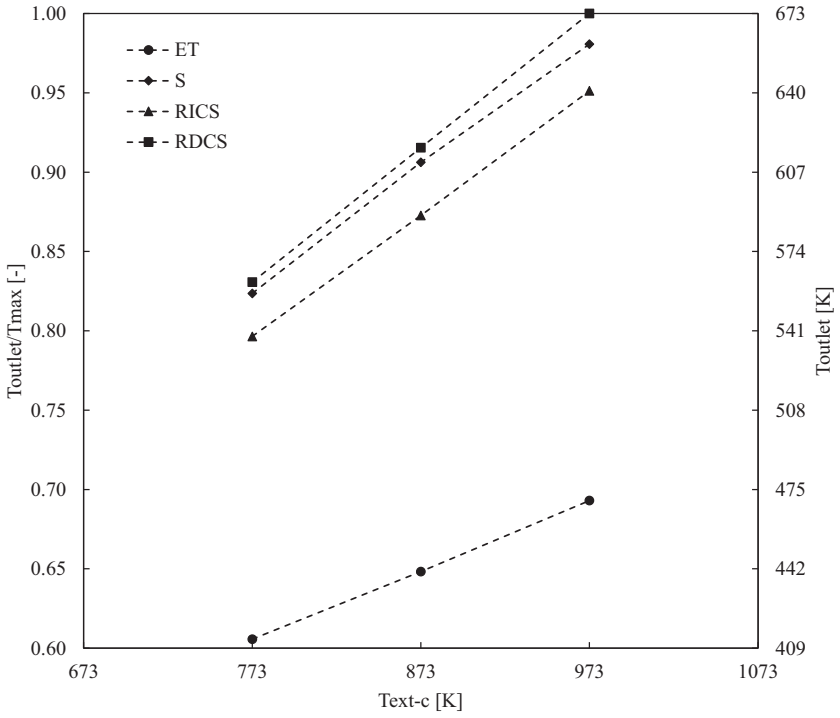

Fig. 9. Experimental outlet air temperatures as a function of the central outer tube temperature (T_{max} = 673 K).

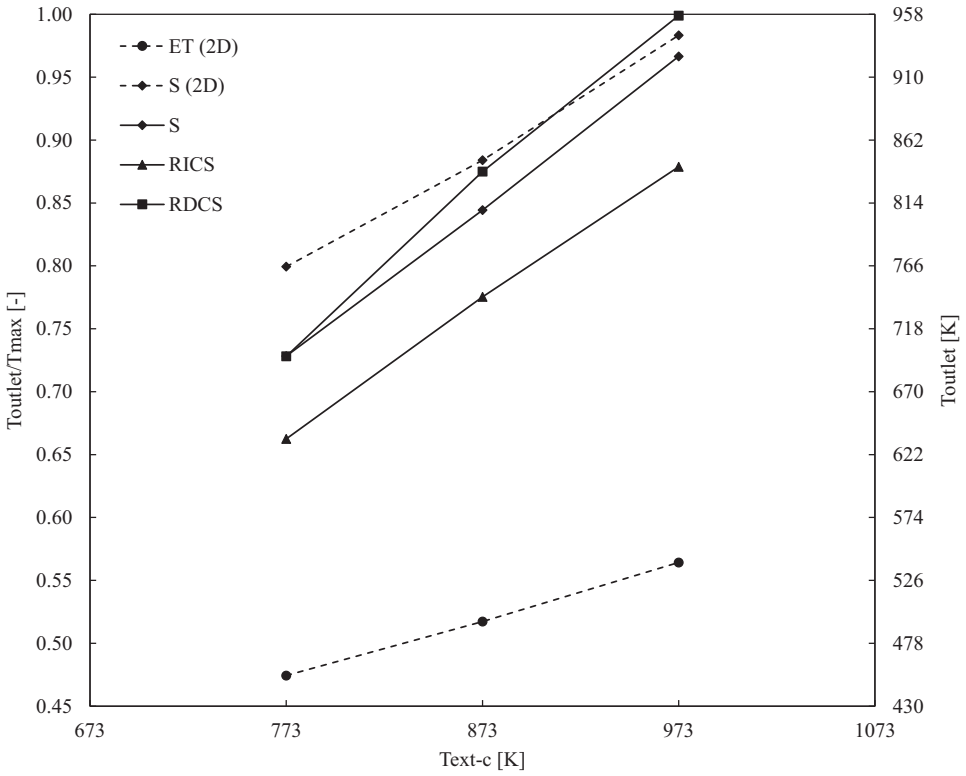

Fig. 10. CFD results: outlet air temperature (from the 3D computational domain) as a function of the central outer tube temperature (T_{max} = 958 K).

5.2.1. Experimental results

Fig. 9 shows the comparison between the air outlet temperatures of the three lattice structures, at three operating temperatures, with respect to the empty tube. The Reynolds number considered for the experimental tests was 745.

The air outlet temperature with the RDCS lattice is higher than in the other cases. Its structure, formed by large cells on the outside, allows radiation to better penetrate through the central region of the lattice, increasing the useful surface area for radiation heat transfer. On the other hand, the worst result was obtained with the RICS lattice which blocks radiation, due to the smaller diameter cells on the outer zone. The S lattice shows an intermediate behaviour. Increasing the wall temperature, the air outlet temperature also increases and the gap between the behaviour of the RDCS lattice with respect to the other ones increases. At higher temperatures, radiation has more influence and the performance of RDCS lattice is increased more than the other lattices. For heat exchangers at high temperature, this ceramic lattice design allows to exploit the radiative heat exchange increasing the performance of the system. This feature is very useful for a porous solar receiver [12].

5.2.2. CFD results

Fig. 10 shows the comparison between the CFD results of the lattice structures under investigation at the Reynolds number of 745. The chart includes also the 2D simulations of ET and S lattice.

According to the experimental tests some considerations can be drawn: (i) the air outlet temperature with the RDCS lattice is higher than the other ones and (ii) by increasing the wall temperature, the difference between the performances of the RDCS and of the other ones increases.

The Standard 2D model provides a higher temperature, due to the porous medium that is simulated as a continuous medium and also it is joined to the wall, favouring conductive heat exchange.

Heat transfer gains and the pressure losses have been calculated, using respectively Eqs. 5 and 6. Table 9 summarizes the results obtained with these two figures of merit for the three lattices.

I terms of heat transfer, the RDCS lattice performed better than the others: it exchanges the highest thermal power, heating air of about 630 K in only 100 mm of pipe. At 873 K, this geometry provides an heat transfer which is 2,15 times higher than the ET, the Standard lattice and the RICS of about 1,96 and 1,56 times respectively. At 773 K, where thermal radiation is not the dominant heat transfer mechanism, the airflow leaves the tube at the same temperature (697 K) for the S and RDCS lattices, which is 1,89 higher than the ET.

Regarding pressure drop, the RICS lattice produces the lowest value among the three lattices, whereas the highest value is obtained by the RDCS lattice with a maximum drop of 20 Pa.

A better understanding of the influence of lattice morphology in the overall heat transfer phenomenon is given in Fig. 11. It shows the temperature contours of the 3D computational domain of the three lattice structures under investigation subjected to a Reynolds of 745 and a wall temperature of 973 K. The inlet air temperature is

Table 9
Gain on heat transfer and increase of pressure drop for S, RICS and RDCS lattices compared to ET.

T_{ext-c}	Lattice	G_Q	$I_{\Delta P}$
[K]	[−]	[%]	[%]
773	S	189%	1′344%
873	S	196%	1′382%
973	S	198%	1′422%
773	RICS	141%	913%
873	RICS	156%	937%
973	RICS	156%	973%
773	RDCS	189%	1′359%
873	RDCS	215%	1′479%
973	RDCS	214%	1′520%

Table 10
Comprehensive data of all the experimental, 2D and 3D results.

Variables			Experimentals				2D simulations							3D simulations		
Re	T_{wall}	Design	T_{inlet}	T_{ext-c}	T_{outlet}	ΔP	T_{inlet}	T_{ext-c}	T_{outlet}	ΔP	T_{in-3D}	T_{out-3D}	ΔP_{3D}	T_{inlet}	T_{outlet}	ΔP
–	K	–	K	K	K	Pa	K	K	K	Pa	K	K	Pa	K	K	Pa
745	773	ET	295	771	408	1.1	293	771	399	1.2	–	–	–	–	–	–
745	873	ET	295	876	436	1.8	293	873	425	1.4	–	–	–	–	–	–
745	973	ET	295	978	466	1.6	293	978	453	1.6	–	–	–	–	–	–
1′490	773	ET	296	774	400	1.5	293	768	397	2.5	–	–	–	–	–	–
1′490	873	ET	296	878	428	1.9	293	874	421	2.9	–	–	–	–	–	–
1′490	973	ET	296	978	458	2.1	293	971	447	3.3	–	–	–	–	–	–
2′235	773	ET	296	772	393	9.0	293	772	398	4.0	–	–	–	–	–	–
2′235	873	ET	298	875	419	14.5	293	870	421	4.6	–	–	–	–	–	–
2′235	973	ET	298	974	445	4.6	293	973	447	5.3	–	–	–	–	–	–
745	773	S	294	774	554	6.7	293	779	544	12.0	316	765	11.25	316	697	14.0
745	873	S	294	875	610	6.5	293	869	592	13.6	322	846	12.84	322	808	16.9
745	973	S	295	972	660	9.3	293	976	649	15.7	329	941	14.80	329	925	20.1
1′490	773	S	294	770	539	16.9	293	775	531	26.5	–	–	–	–	–	–
1′490	873	S	294	875	597	19.1	293	871	576	29.7	–	–	–	–	–	–
1′490	973	S	294	975	650	21.3	293	971	622	33.2	–	–	–	–	–	–
2′235	773	S	293	774	535	31.4	293	772	528	44.6	–	–	–	–	–	–
2′235	873	S	293	876	589	34.5	293	872	573	49.6	–	–	–	–	–	–
2′235	973	S	293	976	635	37.6	293	973	617	54.7	–	–	–	–	–	–
745	773	RICS	296	773	536	7.8	–	–	–	–	–	–	–	316	634	9.8
745	873	RICS	295	873	587	6.2	–	–	–	–	–	–	–	322	742	11.8
745	973	RICS	295	975	640	6.0	–	–	–	–	–	–	–	329	841	14.2
745	773	RDCS	295	775	561	9.4	–	–	–	–	–	–	–	316	697	14.2
745	873	RDCS	295	871	617	9.7	–	–	–	–	–	–	–	322	838	18.0
745	973	RDCS	294	975	673	9.2	–	–	–	–	–	–	–	329	957	21.4

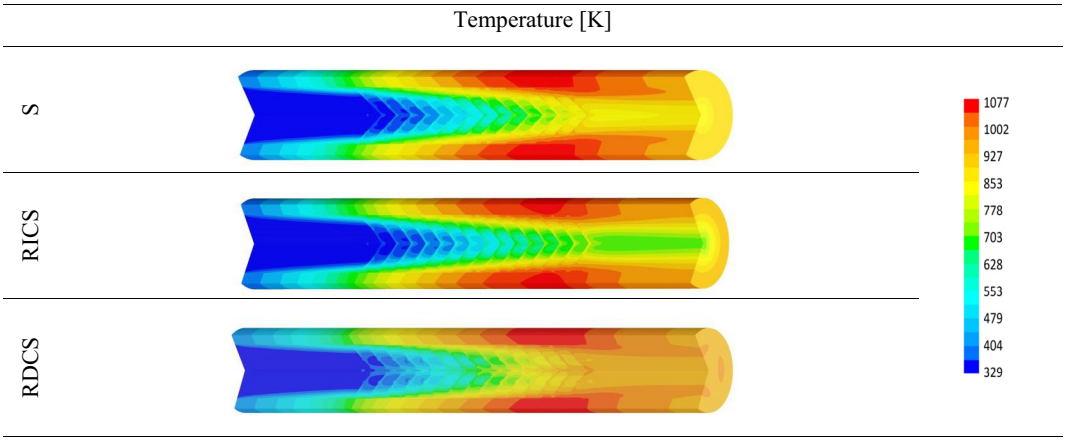

Fig. 11. S, RICS and RDCS: 3D-CFD temperatures of the computational domains.

the same for each case and it is set constant at 329 K (taken from the 2D result), while the velocity profile is fully developed. According to the results obtained, the three lattices show different behaviours in terms of heat transfer regarding: (i) the heat removal from the tube, (ii) the air and lattice temperature distribution and (iii) the air outlet temperature.

To achieve the same central temperature of the tube ($T_{ext\text{-}c}$), different heat fluxes were used: for the S and RDCS lattices the specific power was 17′600 W/m^2 and 18′650 W/m^2 respectively, while for the RICS lattice was 15′110 W/m^2. This means that with the first two lattices it is possible to remove more heat from the tube as indicated by the fact that the specific power to be supplied (to maintain a constant $T_{ext\text{-}c}$) is greater.

Not being in contact with the wall, the lattice is heated by thermal radiation and convection.

In the RICS case, the radiation is mostly blocked on the outer region and does not penetrate towards the tube axis, so the lattice remains colder, and the air consequently, even in the hottest outlet area (Fig. 12). This does not happen in the RDCS, where the particular geometry of the lattice allows radiation to penetrate better, heating even the central struts: cell after cell, the air is almost uniformly heated along the radial direction of the tube. The S lattice has an intermediate behaviour that combines the characteristics of the two.

In the RDCS case, the temperature of the lattice is very similar to the air surrounding it, indicating a good heat transfer between lattice structure and airflow.

The RDCS lattice structure gives the highest air outlet temperature, that is, 957 K (mwa). The RICS lattice has the worst performance and the outgoing air is only at 841 K (mwa). With the S geometry, the outlet air temperature is between the two previous cases: 925 K (mwa).

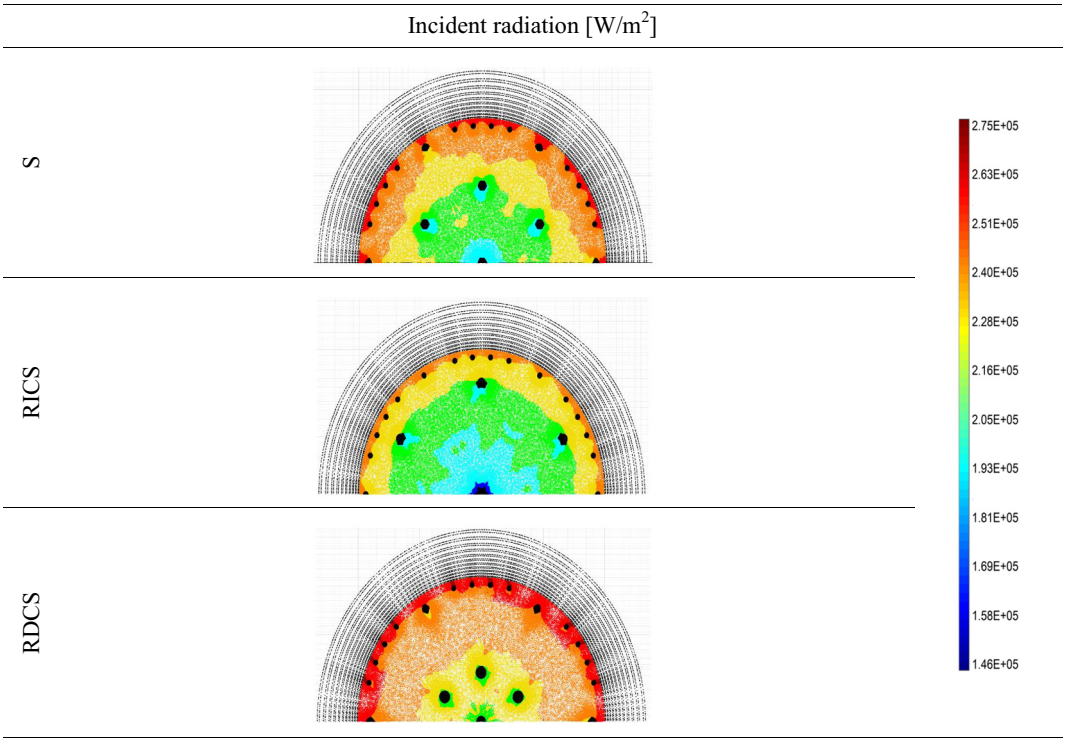

Fig. 12. S, RICS and RDCS: plots of the computed radiative heat flux intensity based on the CFD simulations, on the last cell sections. Black regions represent the solid phase (struts sections).

5.3. Influence of the cells size on radiation flux intensity

To study the influence of the cell size on thermal radiation, the resulting incident radiation flux intensity [W/m^2] on the last cell section was analysed. Fig. 12 shows the plots obtained.

Near the tube the radiative flux is very high, especially in the S and RDCS cases, while in the RICS case it is less intense because a lower heat flux is set. In this area, between the tube and the struts, the highest radiation values were found: the lattice temperature increases due to the radiation and it radiates back on the surrounding areas. This phenomenon is well observable in the RDCS case where there is a peripheral high-flux zone that spreads over the first struts to the tube.

By moving towards the tube axis, the radiation intensity decreases because the first cells act as a shield, blocking its propagation. In the RICS case, this effect is clearly visible; in fact the highest radiative flux zone forms only a small layer, being blocked by very small cells (much solid material). The radiation penetrates better through the S structure, but the best behaviour is shown by the RDCS lattice.

Moving towards the axis, the radiation continues to decrease because it is obstructed by the struts, while in the RICS case near the axis, its decrease is marginal because there are large cells (few solid material).

6. Conclusions

In this work, thermal design and optimization of ceramic lattices has been investigated to maximise the radiative high-temperature heat transfer. The numerical models were designed involving various arrangements of cells and their different sizes and manufactured in Alumina via 3D-printing. Stereolithography (SLA) technique allowed fabricating the green bodies starting from a photopolymeric slurry consisting of acrylic resin TPGDA 56.8 vol% mixed with ceramic powders and UV photo initiator. The green bodies underwent a thermal treatment of debinding and sintering at high temperature, in order to remove the resin and to obtain the mechanical properties of the ceramic. Heat transfer analysis was performed and the thermo-fluid dynamics simulations were successfully validated with respect to experimental tests, concluding that: i) the heat transfer between flowing air and the tube is more effective if a lattice is used, from 160% to 280%; (ii) the RDCS lattice performed better than the other ones, in terms of heat transfer, and (iii) the RICS lattice produces the lowest pressure drop, about 10 Pa, while in the empty tube it is only 2 Pa. RDCS lattice design, large cells outside and small cells inside, allow a higher fraction of thermal radiation to reach the central struts (better than with the other lattices) increasing therefore the heat transfer effectiveness. In the centre of this lattice, the denser array of cell struts is efficiently heated, transmitting in turn their heat to the fluid more efficiently because the fluid is slowed down in this central region. The only counterpart to this efficiency is an increase of the pressure drop, but its absolute value remains very low and does not preclude the use of such a device. For high temperature heat transfer applications, as tubular heat exchanger and solar receivers, this type of ceramic lattice design greatly increases the performances exploiting at best the radiative heat transfer, which is the most efficient in this field.

CRediT authorship contribution statement

M. Pelanconi: Formal analysis, Investigation. **M. Barbato:** Supervision. **S. Zavattoni:** Data curation. **G.L. Vignoles:** Writing - review & editing. **A. Ortona:** Conceptualization, Writing - review & editing.

CRediT authorship contribution statement

M. Pelanconi: Formal analysis, Investigation. **M. Barbato:** Supervision. **S. Zavattoni:** Data curation. **G.L. Vignoles:** Writing - review & editing. **A. Ortona:** Conceptualization, Writing - review & editing.

References

[1] A. Sommers, Q. Wang, X. Han, C. T'Joen, Y. Park, A. Jacobi, Ceramics and ceramic matrix composites for heat exchangers in advanced thermal systems—a review, Appl. Therm. Eng. 30 (11–12) (2010) 1277–1291.
[2] H.J. Strumpf, T.L. Stillwagon, D.M. Kotchick, M.G. Coombs, Advanced industrial ceramic heat pipe recuperators, Heat Recovery Syst. CHP 8 (3) (1988) 235–246.
[3] S. Gianella, D. Gaia, A. Ortona, High temperature applications of Si-SiC cellular ceramics, Adv. Eng. Mater. 14 (12) (2012) 1074–1081.
[4] C. Lewinsohn, M. Wilson, J. Fellows, H. Anderson, Multiscale, ceramic microsystems for heat and mass transfer, Additional Papers and Presentations, 2011 CICMT, 2011, pp. 000001–000007.
[5] Y. Islamoglu, Finite element model for thermal analysis of ceramic heat exchanger tube under axial non-uniform convective heat transfer coefficient, Mater. Des. 25 (6) (2004) 479–482.
[6] Q. Li, G. Flamant, X. Yuan, P. Neveu, L. Luo, Compact heat exchangers: a review and future applications for a new generation of high temperature solar receivers, Renew. Sust. Energ. Rev. 15 (9) (2011) 4855–4875.
[7] M. Scheffler, P. Colombo, Cellular Ceramics: Structure, Manufacturing, Properties and Applications, Wiley-VCH Verlag, 2005.
[8] G. Bianchi, S. Gianella, A. Ortona, Design and additive manufacturing of periodic ceramic architectures, J. Ceram. Sci. Technol 8 (1) (2017) 59–66.
[9] Alberto Ortona, et al., Hetoroporous heterogeneous ceramics for reusable thermal protection systems, J. Mater. Res. 28 (17) (2013) 2273–2280.
[10] A. Ortona, T. Fend, H. Yu, K. Raju, P. Fitriani, D. Yoon, Tubular Si-infiltrated SiCf/SiC composites for solar receiver application—part 1: fabrication by replica and electrophoretic deposition, Sol. Energy Mater. Sol. Cells 132 (2015) 123–130.
[11] A. Ortona, D.H. Yoon, T. Fend, G. Feckler, O. Smirnova, Tubular Si-infiltrated SiCf/SiC composites for solar receiver application – part 2: thermal performance analysis and prediction, Sol. Energy Mater. Sol. Cells 140 (2015) 382–387.
[12] Z. Wu, C. Caliot, F. Bai, G. Flamant, Z. Wang, J. Zhang, C. Tian, Experimental and numerical studies of the pressure drop in ceramic foams for volumetric solar receiver applications, Appl. Energy 87 (2) (2010) 504–513.
[13] B. Esser, J. Barcena, M. Kuhn, A. Okan, L. Haynes, S. Gianella, A. Ortona, V. Liedtke, D. Francesconi, H. Tanno, Innovative thermal management concepts and material solutions for future space vehicles, J. Spacecr. Rocket. 53 (6) (2016) 1051–1060.
[14] P. Dimopoulos-Eggenschwiler, D.N. Tsinoglou, J. Seyfert, C. Bach, U. Vogt, M. Gorbar, Ceramic foam substrates for automotive catalyst applications: fluid mechanical analysis, Exp. Fluids 47 (2009) 209–222.
[15] S. Pusterla, M.C. Barbato, A. Ortona, C. D'Angelo, Numerical study of cell morphology effects on convective heat transfer in reticulated ceramics, Int. J. Heat Mass Transf. 55 (25–26) (2012) 7902–7910.
[16] Z. Wu, C. Caliot, G. Flamant, Z. Wang, Numerical simulation of convective heat transfer between air flow an ceramic foams to optimize volumetric solar air receiver performances, Int. J. Heat Mass Transf. 54 (2011) 1527–1537.
[17] L. Ferrari, M. Barbato, A. Ortona, C. D'Angelo, Convective heat transfer in cellular ceramic: a 3d numerical solution, in: P.J. Meyer (Ed.), In 10th International Conference on Heat Transfer, Fluid Mechanics and Thermodynamics, HEFAT, 2014.
[18] R. Coquard, B. Rousseau, P. Echegut, D. Baillis, H. Gomart, E. Iacona, Investigations of the radiative properties of Al–NiP foams using tomographic images and stereoscopic micrographs, Int. J. Heat Mass Transf. 55 (5) (2012) 1606–1619.
[19] G. Contento, M. Oliviero, N. Bianco, V. Naso, The prediction of radiation heat transfer in open cell metal foams by a model based on the Lord Kelvin representation, Int. J. Heat Mass Transf. 76 (2014) 499–508.
[20] J. Qiu, L.H. Liu, P.F. Hsu, Thermal radiation in subwavelength aluminum foam structures by finite-difference time-domain method, J. Quant. Spectrosc. Radiat. Transf. 158 (2015) 101–110.
[21] G.L. Vignoles, A. Ortona, Numerical study of effective heat conductivities of foams by coupled conduction and radiation, Int. J. Therm. Sci. 109 (2016) 270–278.
[22] Z. Wu, C. Caliot, G. Flamant, Z. Wang, Coupled radiation and flow modeling in ceramic foam volumetric solar air receivers, Sol. Energy 85 (9) (2011) 2374–2385.
[23] S. Haussener, A. Steinfeld, Effective heat and mass transport properties of anisotropic porous ceria for solar thermochemical fuel generation, Materials 5 (1) (2012) 192–209.
[24] A. Bandyopadhyay, S. Bose (Eds.), Additive Manufacturing, CRC Press, 2015.
[25] M.L. Griffith, J.W. Halloran, Freeform fabrication of ceramics via stereolithography, J. Am. Ceram. Soc. 79 (10) (1996) 2601–2608.
[26] C. Hinczewski, S. Corbel, T. Chartier, Ceramic suspensions suitable for stereolithography, J. Eur. Ceram. Soc. 18 (6) (1998) 583.
[27] O. Santoliquido, G. Bianchi, P. Dimopoulos-Eggenschwiler, A. Ortona, Additive manufacturing of periodic ceramic substrates for automotive catalyst supports, Int. J. Appl. Ceram. Technol. 00 (2017) 1–10.
[28] Nabaltec AG, Nabalox aluminas datasheet, http://www.nabaltec.de/download/produkte/NABALOX_1xx-7xx_Datasheet_EN.pdf, Accessed date: 21 January 2018.
[29] H.K. Versteeg, W. Malalasekera, An Introduction to Computational Fluid Dynamics: The Finite Volume Method Approach. Longman Scientific and Technical, Harlow, England, 1995.

[30] ANSYS Inc, ANSYS FLUENT theory guide, http://www.afs.enea.it/project/neptunius/docs/fluent/html/th/node3.htm, Accessed date: 21 January 2018.
[31] M.F. Ashby, A.G. Evans, N.A. Fleck, L.J. Gibson, J.W. Hutchinson, H.N.G. Wadley, Metal foam – A Design Guide, Butterworth-Heinemann, Boston, 2000.
[32] K. Vafai, Handbook of Porous Media, CRC Press, 2005.
[33] Pertti Auerkari, Mechanical and Physical Properties of Engineering Alumina Ceramics, Technical Research Centre of Finland, Espoo, 1996.
[34] F.P. Incropera, D.P. Dewitt, T.L. Bergman, A.S. Lavince, Fundamentals of Heat and Mass Transfer, John Wiley & Sons, Hoboken, NJ, 2007.
[35] ASME J. Heat Transfer 133 (5) (2011) (paper 051701; Heat and Mass Transfer, 2013, 49 (5) 679–694 and 2012, 48 (5) 735–748).